Supporting Information

Self-standing Fe$_3$O$_4$ decorated paper electrode as binder-free trifunctional electrode for electrochemical ammonia synthesis and Zn-O$_2$ batteries

Alankar Kafle[a], Divyani Gupta[a], Ankur Bordoloi[b] and Tharamani C. Nagaiah[a]*

[a]Department of Chemistry, Indian Institute of Technology Ropar, Rupnagar, Punjab 140001, India.

[b]Council of Scientific and Industrial Research – Indian institute of Petroleum, Dehradun, India

*Corresponding author. E-mail address: tharamani@iitrpr.ac.in

Reagents and chemicals used. Hydrochloric acid (HCl, 37%) was purchased from Merck. Nickel chloride (NiCl$_2$.6H$_2$O,97%), ammonium chloride (NH$_4$Cl, 99%), trisodium citrate (Na$_3$C$_6$H$_5$O$_7$), salicylic acid (C$_7$H$_6$O$_3$, 99.5%), sodium nitroprusside (C$_5$FeN$_6$Na$_2$O, 99%), para-dimethylaminobenzaldehyde (p-C$_9$H$_{11}$NO, 99%), ferric nitrate (Fe(NO$_3$)$_3$.9H2O, 98%) and potassium hydroxide (KOH, 85%), sodium hydroxide (NaOH, 98%), hydrazine monohydrate (N$_2$H$_4$.H2O, 99%), sodium hypochlorite solution (NaClO, 4-6%) and hydrogen peroxide solution (H$_2$O$_2$, 5%), zinc acetate (Zn (Ac)$_2$, 98%), mercuric (II) iodide (HgI$_2$) and sodium potassium tartrate (C$_4$H$_4$O$_6$KNa·4H$_2$O), were bought from Loba chemie. Ethanol (C$_2$H$_5$OH, 99.9%), and acetone (CH$_3$COCH$_3$, 99%) were purchased from Rankem. ^{15}NH$_4$Cl (99%) was purchased from Cambridge isotope laboratories. High purity ^{14}N$_2$ (99.999%), ^{15}N$_2$ (99%) and Ar gas (99.999%) and Ar gas (99.999%) cylinders were procured from Sigma. All solutions used in this study were prepared by using deionized water obtained from Millipore system (>15 MΩ).

Physical characterizations. Initially, powder X-ray diffraction was carried out by using PANalytical X'PERT pro diffractometer with Cu-Kα radiation (λ=0.1542 nm, 40kV, 40mA) under the 2θ range of 5-80° at a scan speed of 2° per minute and a proportional counter detector for structural investigation of catalysts. Further, the morphology of the catalysts were studied using number of techniques including scanning electron microscopy (SEM, JEOL, JSM-6610LV), field emission-scanning electron microscopy (FE-SEM, Hitachi, Japan, SU8010) and transmission electron microscopy (HR-TEM, JEOL, Jem 2100 plus) where the high-resolution TEM (HR-TEM) images were obtained at 200 kV. The oxidation states of elements in the catalyst were studied with X-ray photoelectron spectroscopy XPS by using Thermo scientific NEXSA surface analysis with a

micro-focused (400 μm, 72 W, 12000 V) monochromatic Al Kα (1486.6 eV) a hemispherical analyser and 128 channel plate detectors under ultrahigh vacuum (UHV 8-10 mbar). The obtained spectra were calibrated with C 1s spectra. Quantification of various products formed during NRR were tested using an (SEC2000-DH) UV-Vis Spectrometer.

Electrochemical characterizations. All the electrochemical investigations were carried out in a single compartment electrochemical cell during ORR and OER. On the other hand, for NRR, the electrochemical characterizations were executed in a home made two compartment H-cell, separated by a Nafion N117 membrane under ambient conditions of temperature and pressure. Prior fitting the membrane into the H-cell, cleaning of membrane was done by initially boiling it in deionized water (>14 MΩ) for 30 min., and then in H_2O_2 (5%) solution for another 30 min. at 80 °C, after which it was finally boiled in 0.05 M H_2SO_4 for continuous 1 h. A typical three electrode electrochemical cell-setup comprising of a working electrode (WE), a home-made double junction Hg/HgO/1M NaOH reference electrode (RE) and Pt wire counter electrode (CE) was used for electrochemical measurements in 1 M KOH (for ORR/OER) and 0.1 M KOH (for NRR) electrolyte solution. Autolab 302N modular potentiostat/galvanostat was utilised to perform RDE experiments and further analysed by NOVA 1.11 software under the hydrodynamic conditions at different rotation rates by using a speed controlling unit (AFMSRC, Pine research instrument Inc., USA). All other investigations were done by means of Biologic VSP 300 Potentiostat including linear sweep voltammetry (LSV), chronoamperometry, electrochemical impedance spectroscopy (EIS) and cyclic voltammetry (CV).
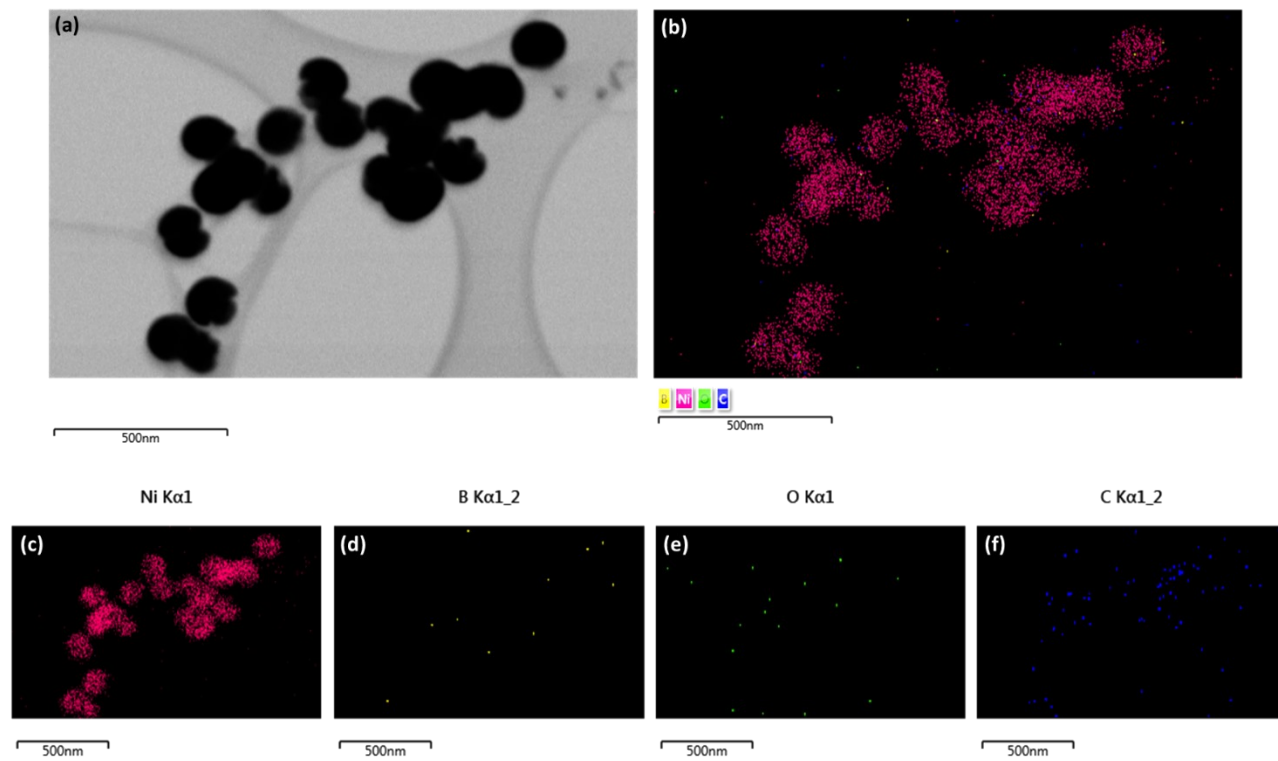
Fig. S1 TEM elemental dot mapping images for (a) all elements and separately for (b) Ni, (c) B, (d) C and (e) O of NiB-CP electrode.
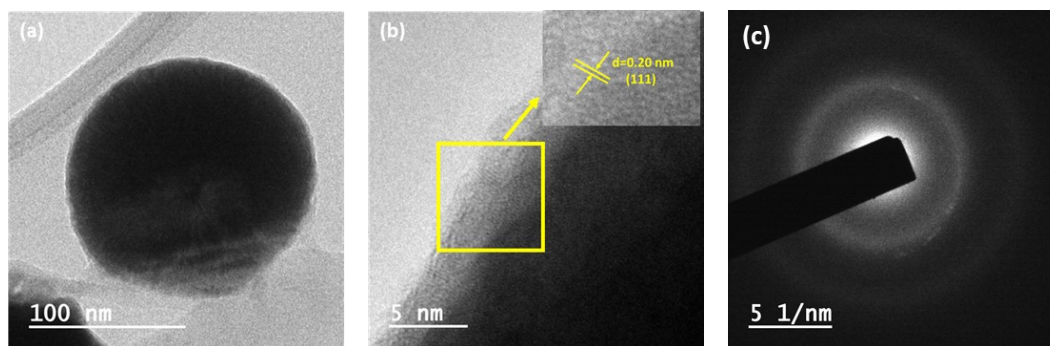

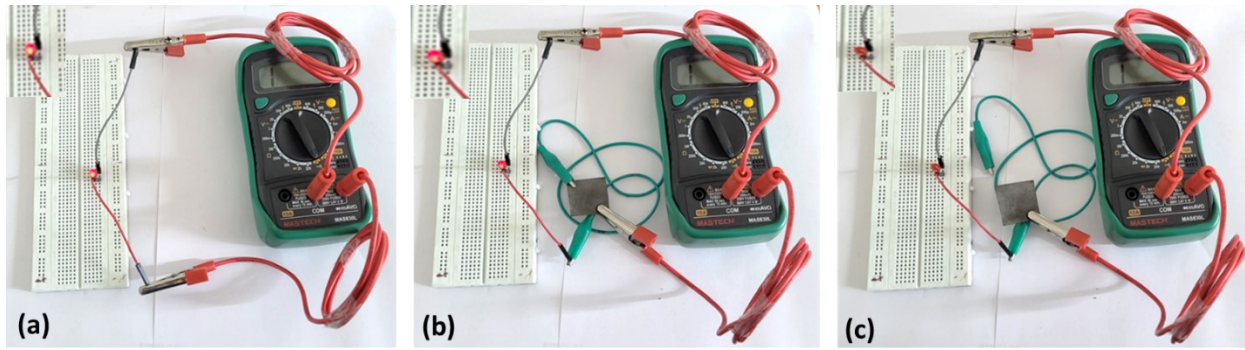**Fig. S2** (a) TEM, (b) HR-TEM image and (c) SAED pattern of NiB-CP electrode.

Fig. S3 Photograph of lighting LED (a) directly by multimeter, (b) through NiB-CP and (c) photograph of light off LED after disconnection. (Inset: zoomed part of the LED bulb).

Conductivity measurements by four probe method[1]

The electrical conductivity of the NiB-CP was measured by four probe method. The Ni-CP paper was placed below the four probes then a fixed amount of current was applied on it and the corresponding potential was recorded. The resistivity ρ_o is obtained as:

$$\rho_o = \frac{V}{I} 2\pi s$$

Where,

V = floating potential difference between the inner probes,

I = current through the outer pair of probes and

s = spacing between point probes

The resistivity for thin film is corrected as:

$$\rho = \frac{\rho_o}{G_7\left(\frac{w}{s}\right)}$$

$$G_7(w/s) = \frac{2s}{w} ln2$$

Where, s = spacing between probes = 0.2 cm and

w = thickness of NiB-CP electrode = 0.027 cm

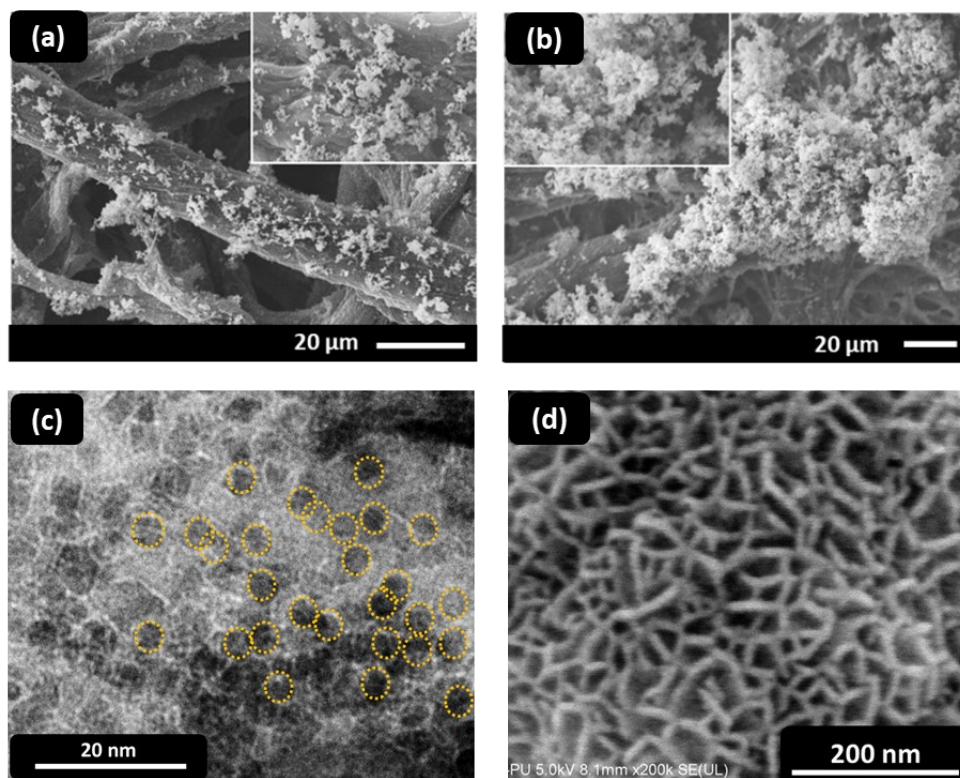And finally, the conductivity was calculated from the reciprocal of the resistivity.

Fig. S4 SEM images of (a) Fe$_3$O$_4$-60/NiB-CP and (b) Fe$_3$O$_4$-80/NiB-CP electrodes. (c) HR-TEM image, (d) FE-SEM of Fe$_3$O$_4$-70/NiB-CP showing porous framework in Fe$_3$O$_4$ nanospheres.
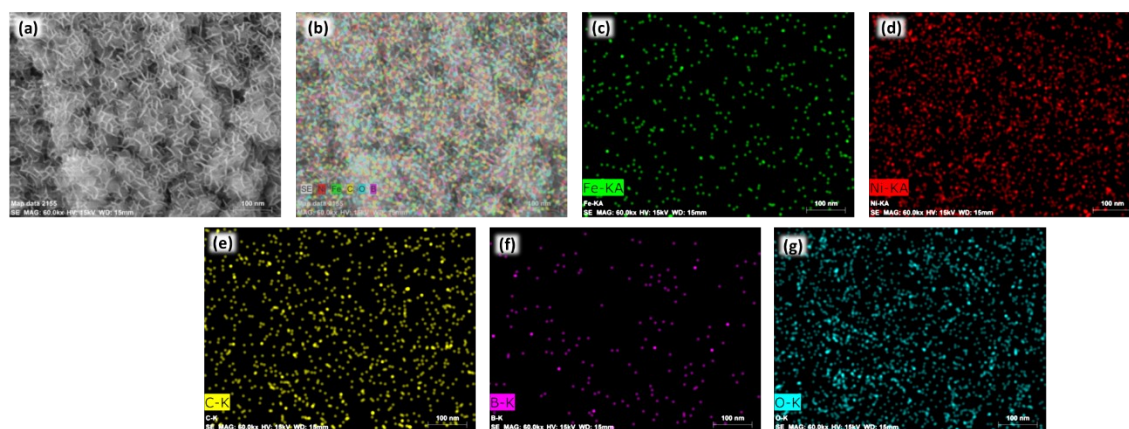

Fig. S5 (a) Scanned area for elemental dot mapping images of (b) all elements and separately for (c) Ni, (d) Fe (e) B, (f) C and (g) O of Fe$_3$O$_4$-70/NiB-CP electrode.

Table S1. Elemental analysis of Fe$_3$O$_4$-70/NiB-CP electrode.

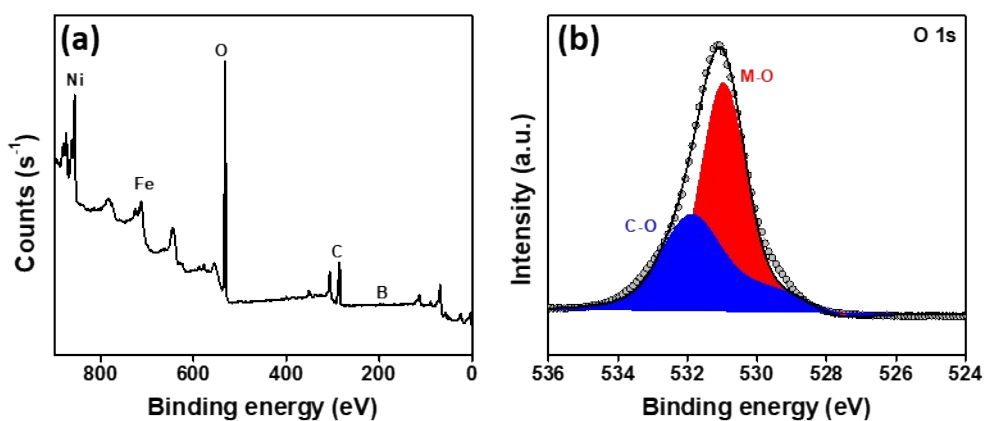| S.No.	Elements	EDS Analysis (mass %)	MP-AES Analysis (mass %)
1	Nickel	46.5	45.64
2	Iron	3.38	5.27
3	Carbon	20.29	-
4	Oxygen	19.89	-

Fig. S6 The XP spectra of Fe$_3$O$_4$-70/NiB-CP (a) Full survey scan and (b) deconvoluted spectra of O1s.
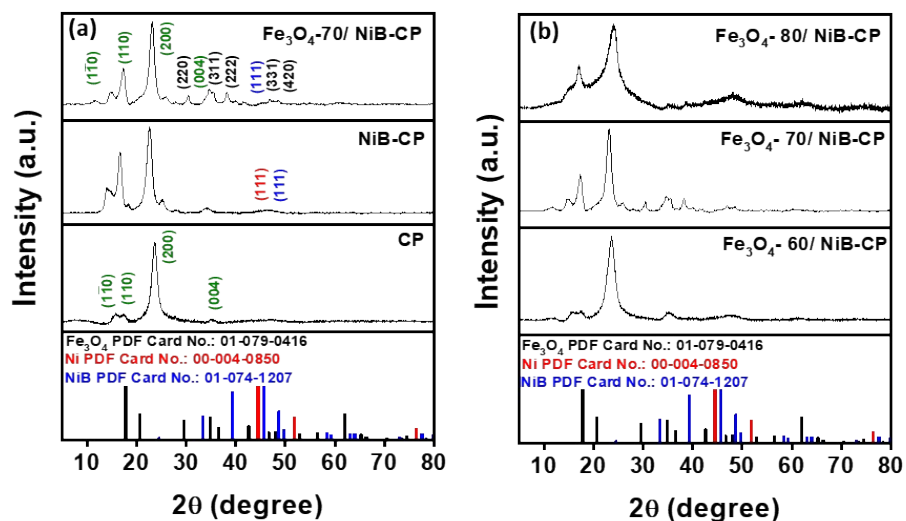
Fig. S7A The P-XRD pattern of (a) bare CP, NiB-CP, and Fe_3O_4-70/NiB-CP and (b) Fe_3O_4-60/NiB-CP, Fe_3O_4-70/NiB-CP and Fe_3O_4-80/NiB-CP electrodes.

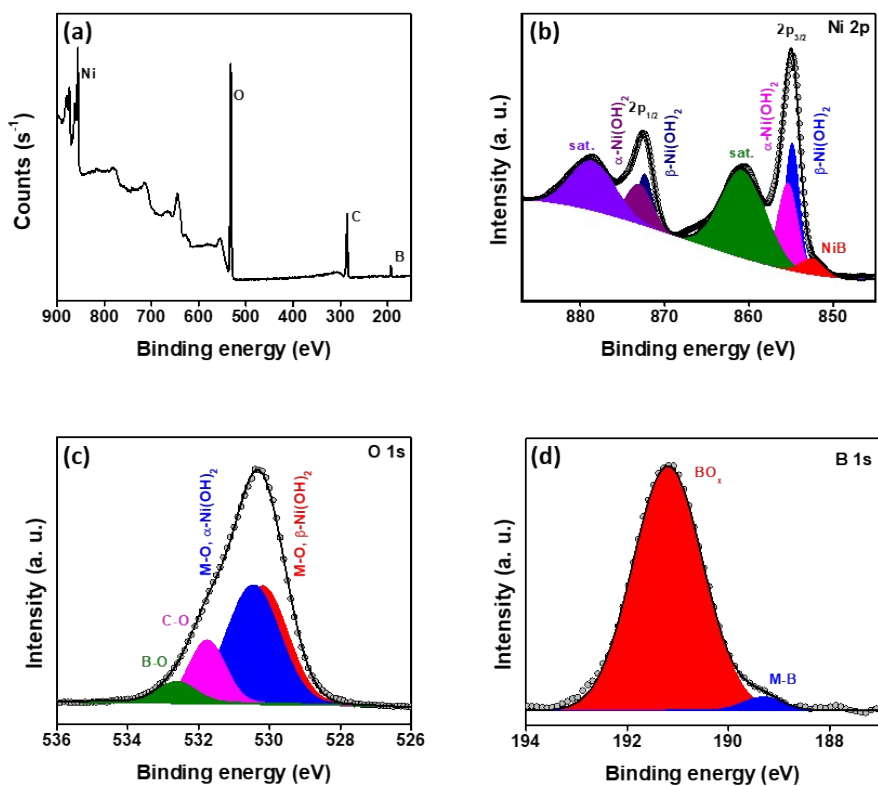**Fig. S7B** The XP spectra of NiB-CP (a) Full survey scan and deconvoluted spectra of (b) Ni 2p, (c) O 1s and (d) B 1s.

Quantification of Ammonia[2]

By Indophenol blue method: The amount of ammonia formed during electrochemical reduction was quantified UV-Visible spectrophotometrically by Indophenol blue method. In detail, 2 mL of electrolyte was taken after the reduction and 2 mL of salicylic acid & sodium citrate (5% each) solution in 1M KOH followed by 1 mL of 0.05 M NaClO and 0.2 mL of 1% $C_5FeN_6Na_2O \cdot 2\ H_2O$ were added and left for 2 hrs for complete color development. finally, the UV-Vis absorption spectra were recorded at a wavelength of 655 nm. The concentration–absorbance calibration curve was generated with the help of standard NH_4Cl solution with known NH_4^+ concentrations of 0.1, 0.2, 0.4, 0.8, 1.0 and 2.0 µg mL^{-1} and from which the ammonia was determined. The rate of ammonia formation was determined according to

$$Yield\ rate(\mu g\ cm^{-2}\ h^{-1}) = \frac{V \times C_{NH_3}}{t \times m_{cat.}}$$

Here, C_{NH3} is the measured NH_3 concentration, V the volume of electrolyte, t the time of the reduction reaction and m_{cat} is the mass of the catalyst loaded onto the electrode.

Similarly, its Faradaic efficiency (F.E.) was calculated as

$$F.E.\,(\%) = \frac{3 \times F \times V \times C_{NH3}}{17 \times Q}$$

Where F is the Faraday constant and Q is the total amount of charge passed through the electrodes during the electrolysis.

By Nessler's reagent method:[3] The amount of NH_3 quantified by Indophenol blue method was further validated by performing Nessler's test. The Nessler's reagent was prepared by mixing 2.5 g of mercuric iodide into 5 mL aq. solution of potassium iodide (2 g in 5 mL deionized water)

which was further diluted to 20 mL by with deionized water and finally 4 g of NaOH was added into it. The electrolyte solution (5 mL) was collected after e-NRR and 0.25 mL of sodium potassium tartrate (500 g L^{-1}) followed by 0.25 mL of Nessler's reagent was added into it and left for 10 minutes for color development. And finally, UV-Vis. absorption measurement was performed at λ=420 nm. The calibration curve was developed by using standard NH$_4$Cl solution having concentrations of 0.1, 0.2, 0.4, 0.8, and 1.0 μg mL^{-1} in the same way.

Quantification of hydrazine *By Watt-Chrisp method:*[2] The hydrazine formed during the electrolysis was quantified UV-visible spectrophotometrically by Watt and Chrisp method by applying coloring solution composed of p-C$_9$H$_{11}$NO (0.4 g) in HCl (concentrated, 2 mL) and C$_2$H$_5$OH (20 mL). After electrolysis, 2 mL of electrolyte taken from cathodic chamber was mixed with 2ml of coloring solution and kept for 20 minutes in room temperature for color development. Finally, the N$_2$H$_4$ was quantified UV-visible spectrophotometrically with the help of calibration curve generated by recording absorbance at 455 nm by taking standard hydrazine solution of concentrations of 0.1,0.2, 0.4, 0.8 and 1.0 μg mL^{-1} in 0.1 M KOH.

TOF calculations for the catalyst during e-NRR:

$$Turnover\ frequency\ (TOF) = \frac{Turnover\ number\ (TON)}{Time\ (h)}$$

$$(TON) = \frac{NH_3 yield\ (mg)}{Catalyst\ loading\ (mg)}$$

Isotope labelling experiments: In order to perform the isotope labelling experiment, ^{15}N$_2$ (Sigma-Aldrich 99 atom% ^{15}N) was taken as the feeding gas which was passed through

alkaline KMnO$_4$ followed by dilute H$_2$SO$_4$ solution in order to eliminate the N-containing impurities before purging to cell and a fixed amount of gas (20 mL gas in the interval of the 15 minutes) was supplied during the electrolysis at -0.1 V vs. RHE for 1 h. The electrolyte (25) was taken out after electrolysis and acidified with 1M HCl solution and finally concentrated to 2 mL. Then, 0.9 ml of the concentrated solution was mixed with 0.1 ml of DMSO- d6 as an internal standard and performed ^{1}H nuclear magnetic resonance measurements (^{1}H NMR) with water suppression.
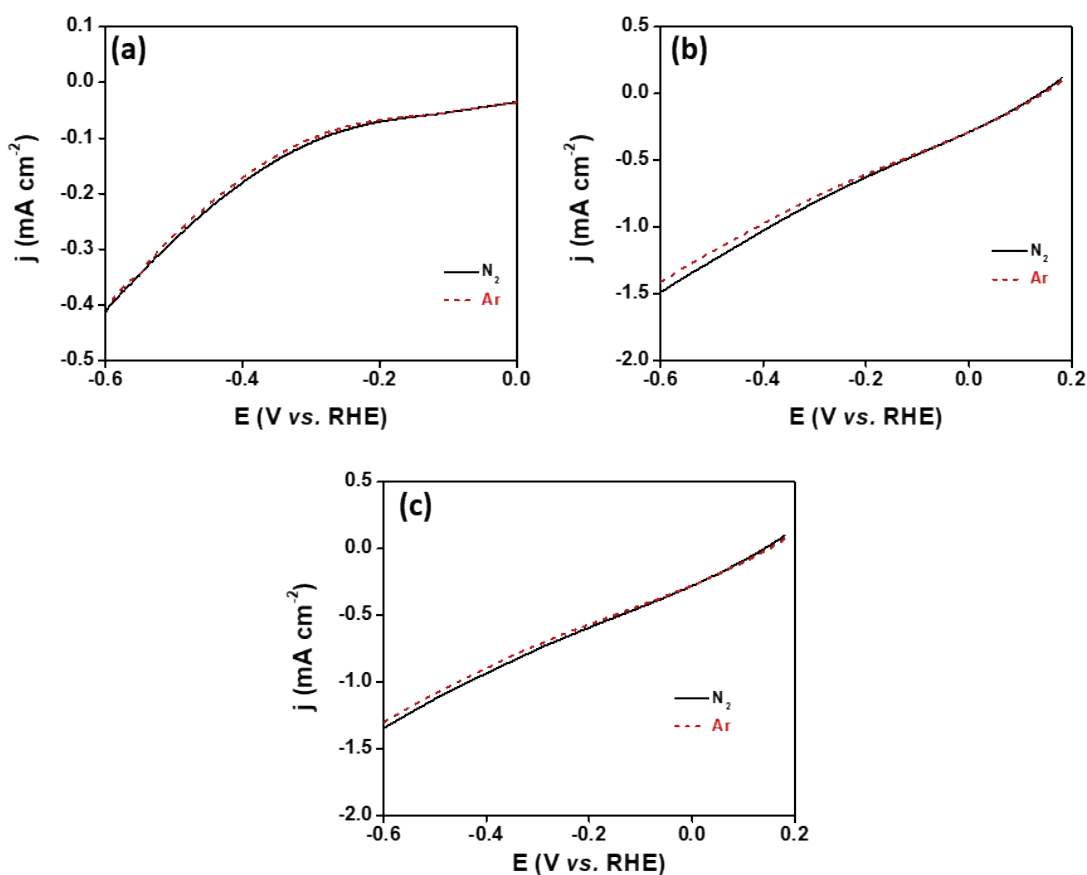
Fig. S8 LSV curves of (a) NiB-CP (b) Fe$_3$O$_4$-60/NiB-CP and (c) Fe$_3$O$_4$-80/NiB-CP electrodes recorded in Ar and N$_2$ saturated 0.1 M KOH.
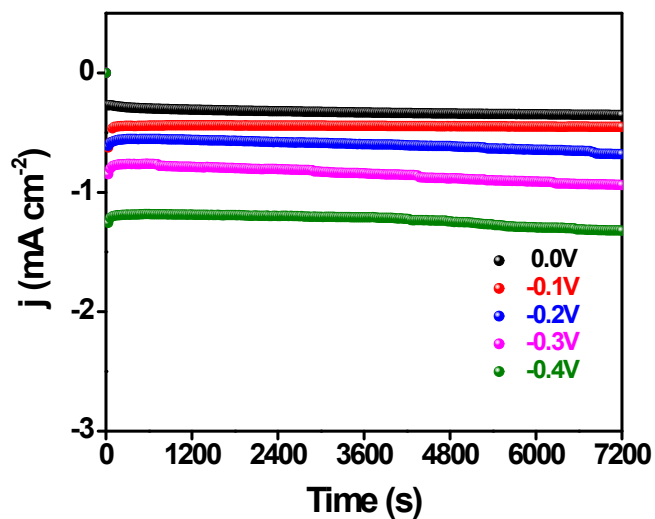
Fig. S9 Chronoamperometric curves of Fe_3O_4-70/NiB-CP at different potentials.

Table S2. Comparison of onset potential and net current density of different composites extracted from Fig. 2a and Fig. S7.

S. No.	Composite	Onset potential (V *vs.* RHE)	Net current density (j_{Ar}-j_{N2}) (mA cm^{-2}) @-0.1 V *vs.* RHE
1	Fe_3O_4-60/NiB-CP	-0.09	0.020
2	Fe_3O_4-70/NiB-CP	-0.05	0.024
3	Fe_3O_4-80/NiB-CP	-0.11	0.018
4	NiB-CP	-0.21	-
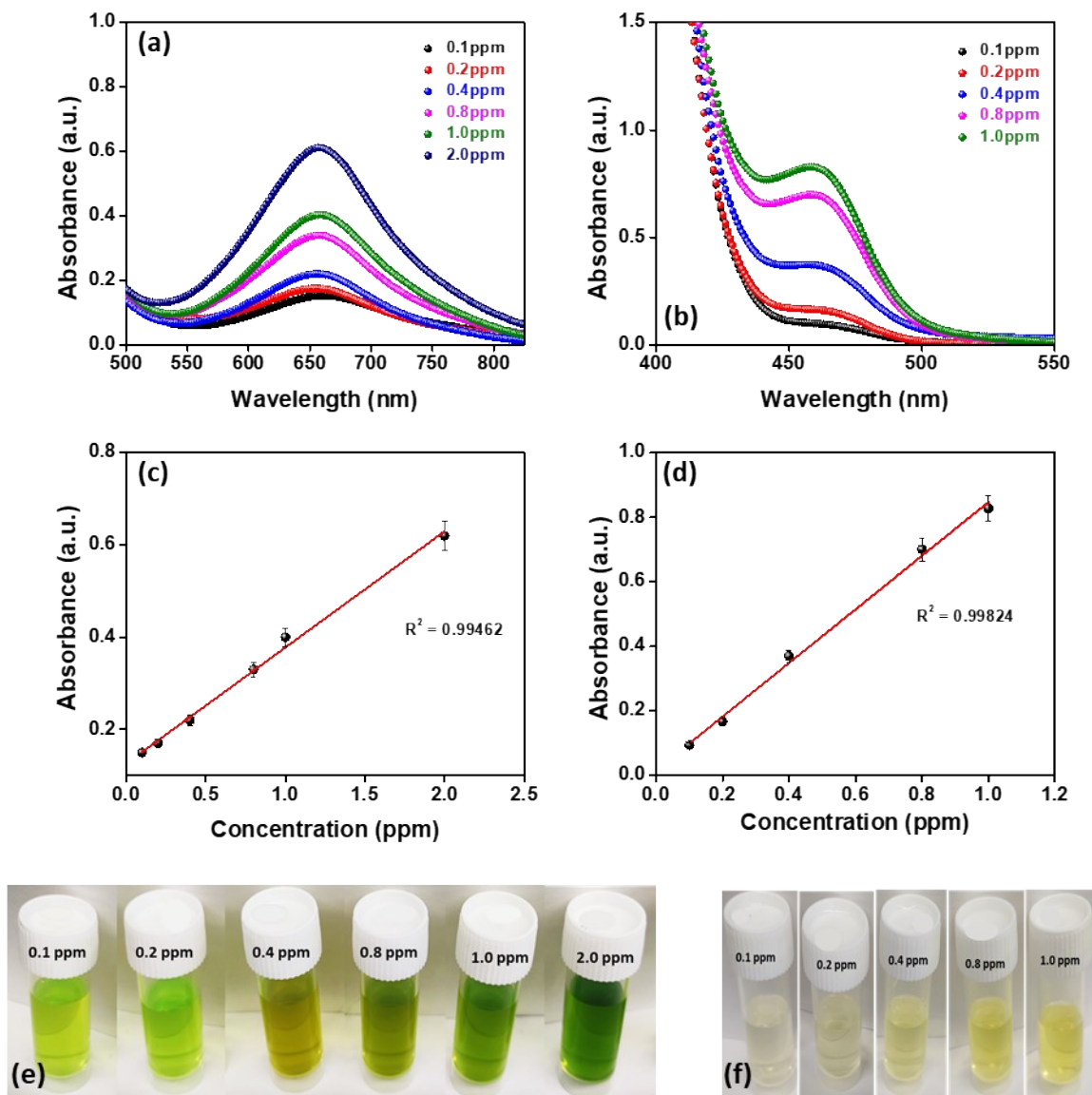
Fig. S10A UV-Vis spectrum of various known concentration standard (a) NH$_3$ solutions quantified using Indophenol blue method, (b) N$_2$H$_4$ solutions by Watt and Chrisp method and (c-d) & (e-f) their corresponding calibration curves and images captured during color development before UV-Vis. analysis.
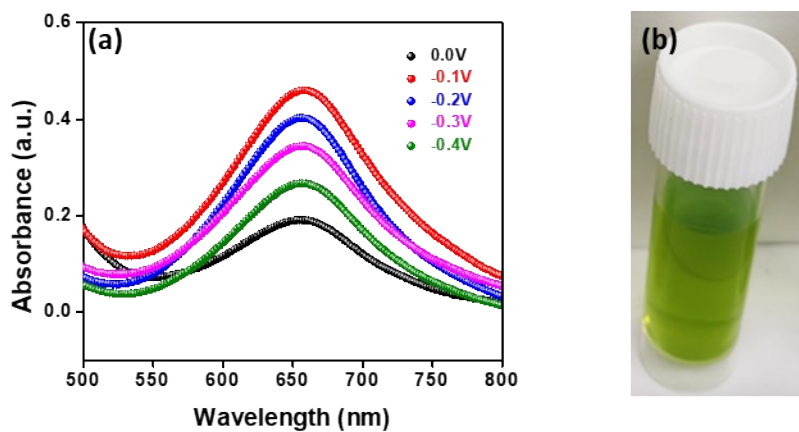
Fig. S10B (a) UV-vis spectrum of Fe_3O_4-70/NiB-CP obtained of the electrolyte sample after 2 h chronoamperometry at different potentials in N_2 saturated 0.1 M KOH electrolyte. (b) Photograph captured upon color development in electrolyte solution after 2h electrolysis at -0.1 V.
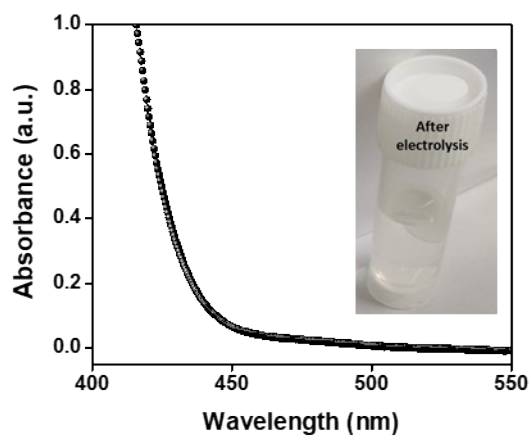
Fig. S10C UV-Vis spectra for N_2H_4 solutions obtained by Watt and Chrisp method of the electrolyte sample after 2 h chronoamperometry at -0.1 V *vs.* RHE (inset: Photograph captured upon color development in electrolyte solution after 2h electrolysis at -0.1 V).
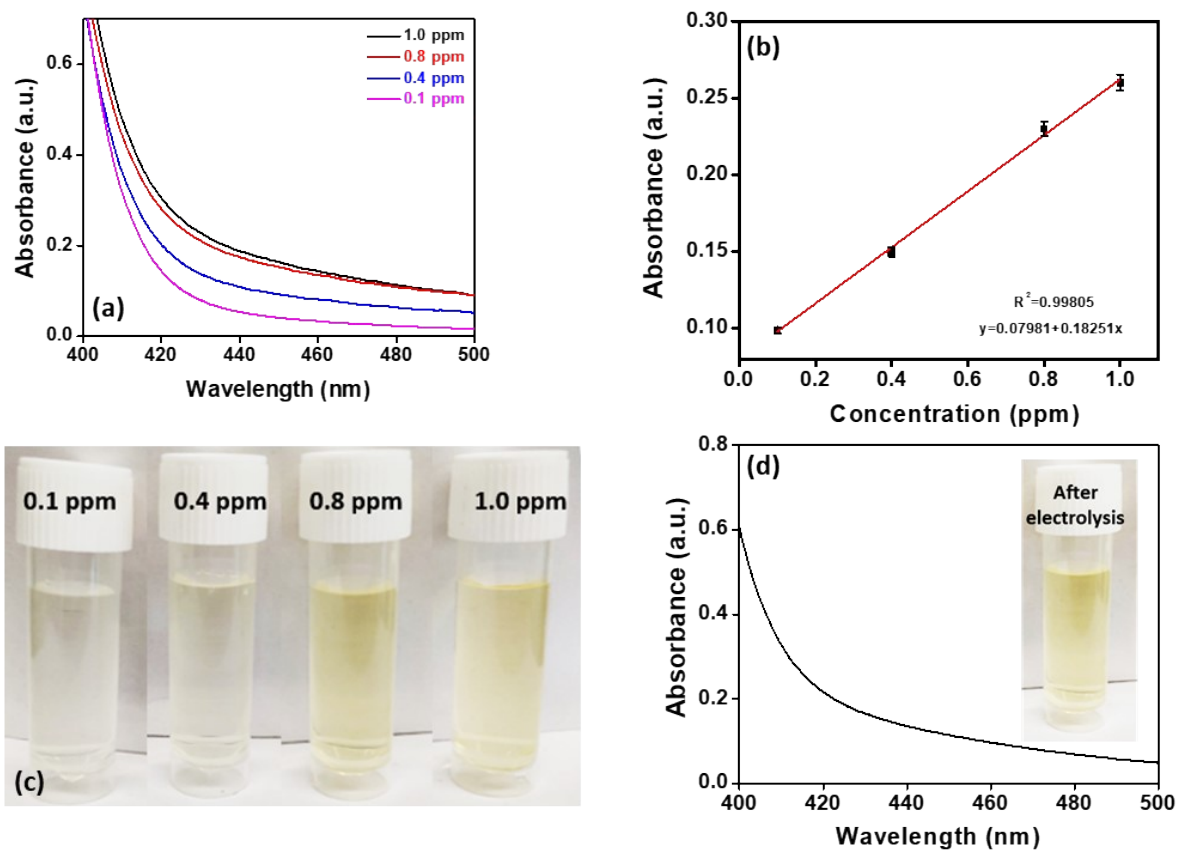

Fig. S11 (a) Standard UV-Vis. curves for NH_4^+ solutions (different concentrations) via Nessler's reagent test and (b) corresponding calibration curve extracted from (a). (c) Images showing color development of standard solutions with different NH_4^+ concentrations after Nessler's test. (d) UV-Vis. absorbance curve for electrolyte solution collected after NRR by Fe_3O_4-70/NiB-CP in N_2-saturated 0.1 M KOH during Nessler's test.
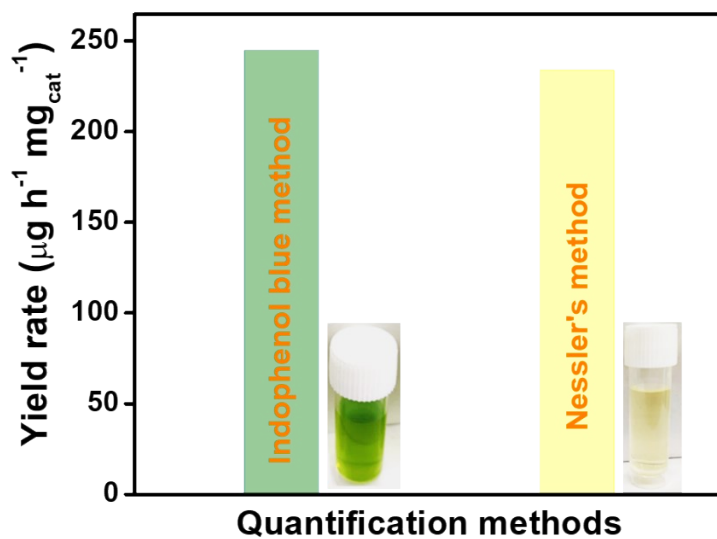
Fig. S12 Bar graph comparison of NH$_3$ yield obtained after NRR by Fe$_3$O$_4$-70/NiB-CP at -0.1 V (*vs.* RHE) by different quantification methods.

Table S3. NH$_3$ yield obtained from different quantification techniques for Fe$_3$O$_4$-70/NiB-CP at -0.1 V.

Method	Yield rate (μg h^{-1} mg$^{-1}_{cat.}$)
Indophenol blue	245
Nessler's reagent	234

Table S4. Comparison of Faradic efficiency and yield rate during NRR of flexible electrodes with other reported literature

S.No.	Composite	Substrate	F.E. at V *vs.* RHE	Yield	Electrolyte	Ref.
1	N-free carbon cloth	Carbon cloth	6.92% at −0.3 V	2.59×10^{-10} mol cm^{-2} s^{-1}	0.1 M Na_2SO_4 + 0.02 M H_2SO_4	[4]
2	MoN/CFC	Carbon cloth	12.84% at −0.45 V	107.3 µg h^{-1} cm^{-2}	0.1 M KOH	[5]
3	S/N co-doped carbon cloth (CC)	Carbon cloth	8.11% at −0.3 V *vs.* RHE)	9.87×10^{-10} mol s^{-1} cm^{-2}	0.05 M H_2SO_4	[6]
4	p-Fe_2O_3/CC	Carbon cloth	7.69% at −0.4 V	6.78µg h^{-1} cm^{-2}	0.1 M Na_2SO_4	[7]
5	BiNPs@NF	Nickel foam	6.3% at -0.5V	9.3×10^{-11} mol s^{-1} cm^{-2}	0.5 M K_2SO_4	[8]
6	SnS_2@Ni	Nickel foam	10.8% at −0.5 V	9.17×10^{-10} mol s^{-1} cm^{-2}	0.1 M Na_2SO_4	[9]
7	Fe–MoS_2/CC	Carbon cloth	10.8% at −0.1 V	12.5 µg h^{-1} cm^{-2}	0.1 M KOH	[10]
8	VN/CC	Carbon cloth	3.58%) at −0.3 V	2.48×10^{-10} mol^{-1} s^{-1} cm^{-2}	0.1 M HCl	[11]
9	MoS_2-x	Carbon cloth	`10% at 0.3 V overpotential	0.63 mmol/h/g	0.01 M H_2SO_4	[12]
10	Fe_3O_4-70/NiB-CP	Cellulose paper	4.32% at -0.1 V	245 µg h^{-1} mg_{cat}^{-1}	0.1 M KOH	This work

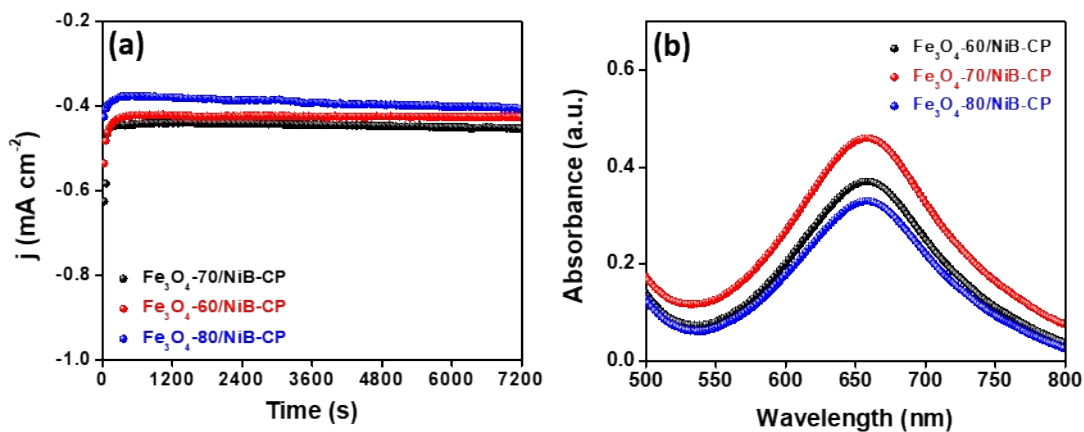**BiNPs@NF:** bismuth nanoparticle @ nickel foam

Fig. S13 (a) Chronoamperometric curves of Fe_3O_4-60/NiB-CP, Fe_3O_4-70/NiB-CP and Fe_3O_4-80/NiB-CP at -0.1V *vs.* RHE and (b) corresponding UV-vis spectrum in N_2 saturated 0.1 M KOH electrolyte.

Table S5. Comparison of faradic efficiency and yield rate during NRR of different electrodes.

S.No.	Composite	F.E. (%)	Yield ($\mu g\ h^{-1}\ mg^{-1}$)
1	Fe_3O_4-60/NiB-CP	2.56	144
2	Fe_3O_4-70/NiB-CP	4.32	245
3	Fe_3O_4-80/NiB-CP	2.24	111
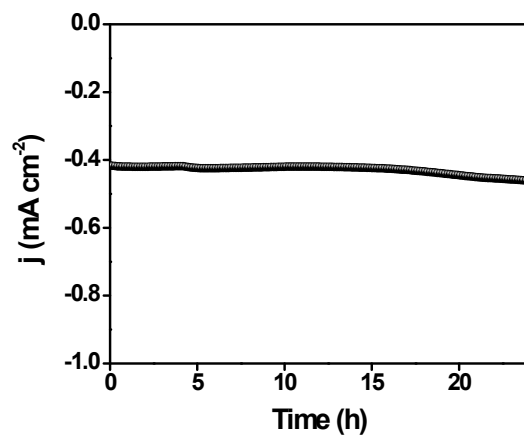
Fig. S14A Chronoamperometric curve of Fe$_3$O$_4$-70/NiB-CP in nitrogen saturated 0.1M KOH.
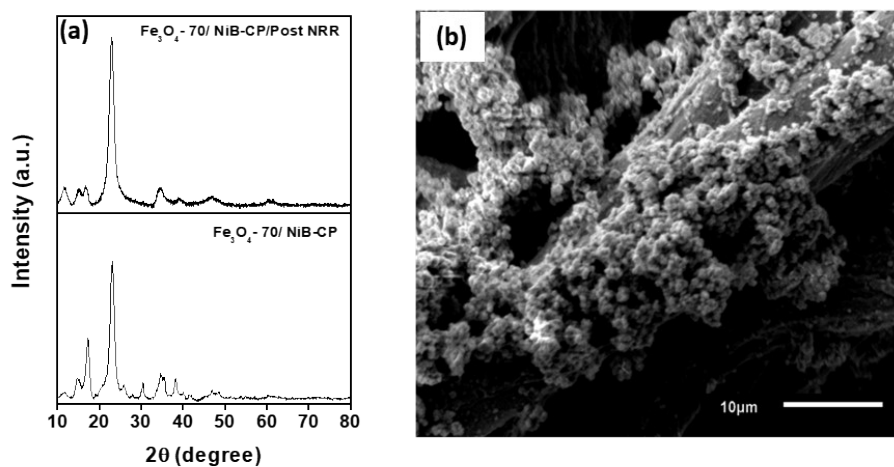
Fig. S14B (a) The diffraction pattern of Fe$_3$O$_4$-70/NiB-CP electrode before and after stability study during NRR. (b) SEM image of Fe$_3$O$_4$-70/NiB-CP electrode after stability study duri NRR.
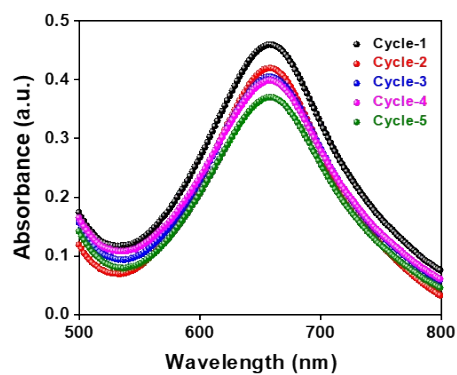

Fig. S15 UV-vis spectrum of Fe$_3$O$_4$-70/NiB-CP for five different cycles in N$_2$ saturated 0.1 M KOH electrolyte.
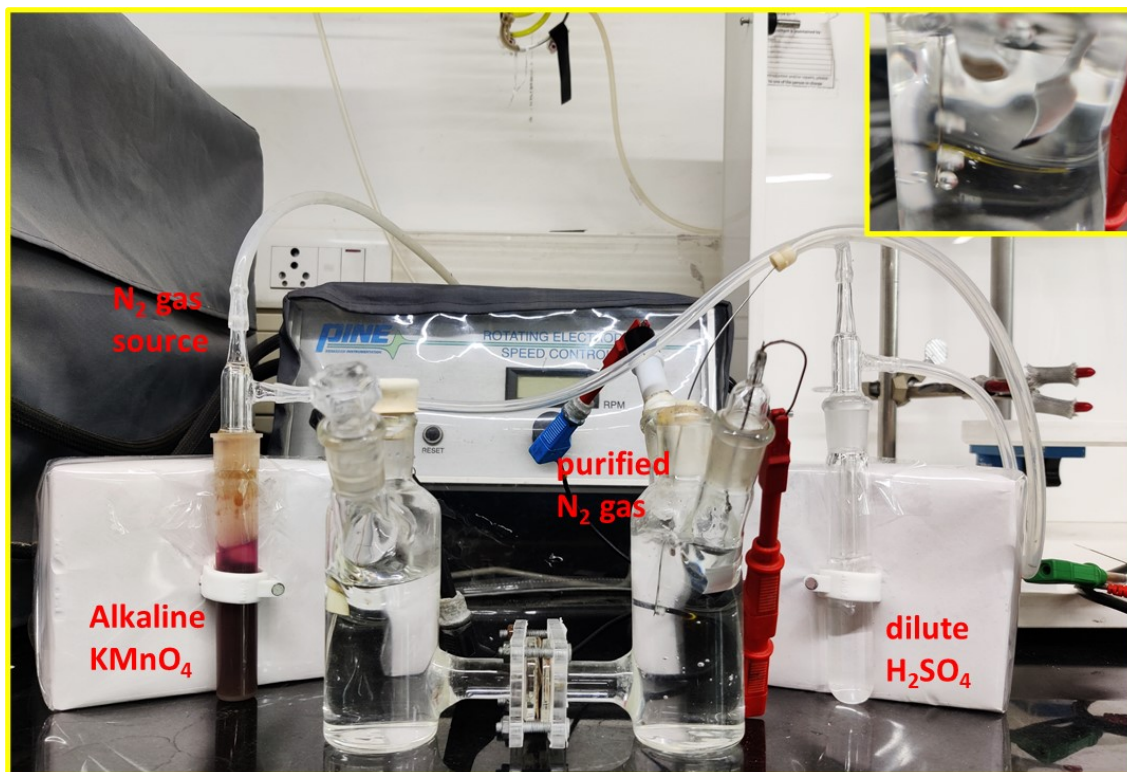
Fig. S16 Image of H-cell setup prior to NRR measurements for purification of gas-streams passing through $KMnO_4$ and acid trap (inset: zoomed part of cathodic compartment showing paper electrode).

Nitrate (NO_3^-) and nitrite (NO_2^-) determination [13]:

In order to determine the trace amount of NO_3^- present in the electrolyte (i.e. 0.1 M KOH), UV-Vis. spectrophotometry was applied by considering the λ_{max} at 220 nm whereas the quantification of nitrites was carried out by through formation of a reddish purple azo dye produced at pH 2 - 2.5 by coupling diazotized sulfanilamide with N - (1-naphthyl) - ethylenediamine dihydrogen chloride (NEDA). The photometric measurement of the colored dye is done at 540nm.
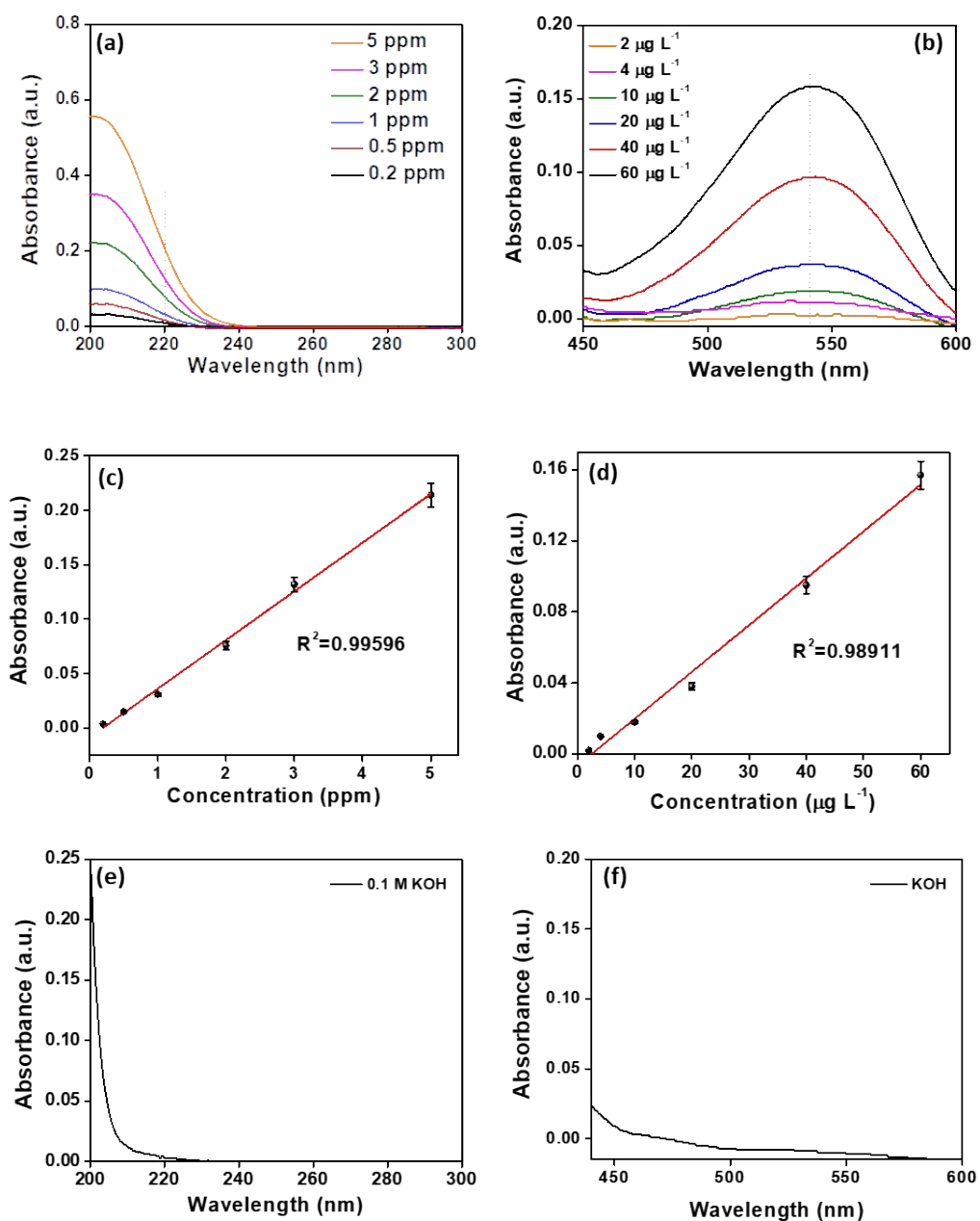
Fig. S17 UV-Vis. absorbance curves for standard (a) NO_3^- and (b) NO_2^- solutions and (c)-(d) corresponding calibration curves. Quantification of (e) NO_3^- and (f) NO_2^- in 0.1 M KOH electrolyte solution.
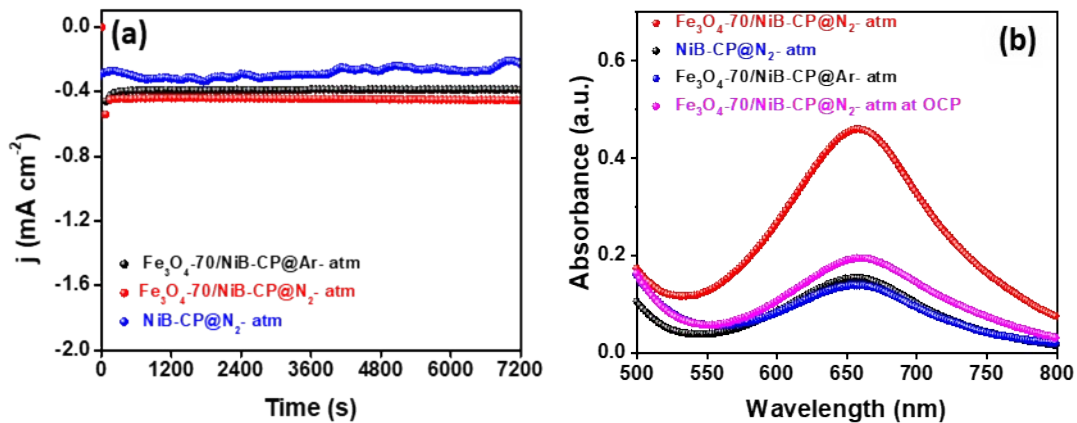
Fig. S18 (a) Chronoamperometric curves of Fe_3O_4-70/NiB-CP in N_2/Ar saturated electrolyte and NiB-CP in N_2 saturated 0.1 M KOH at -0.1 V *vs.* RHE and (b) corresponding UV-vis spectrum including of Fe_3O_4-70/NiB-CP at OCP in N_2 saturated 0.1 M KOH electrolyte.

Table S6. Comparison of overpotential and tafel slope for different composites towards OER.

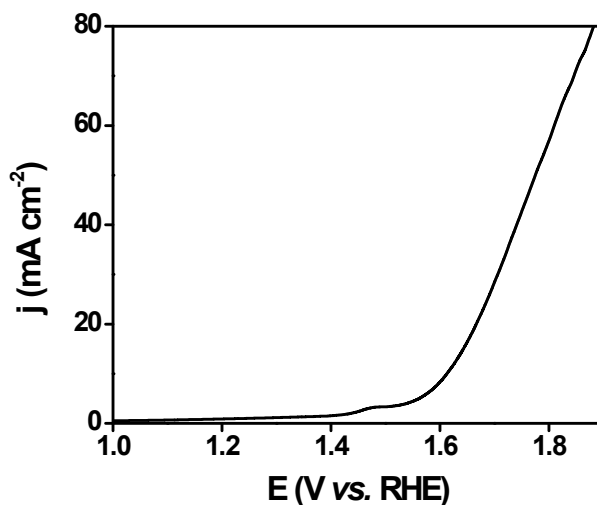| S.No.	Composites	Overpotential@10 mA cm^{-2} (mV)	Tafel slope (mV dec^{-1})
1	Fe_3O_4-60/NiB-CP	180	131
2	Fe_3O_4-70/NiB-CP	210	79
3	Fe_3O_4-80/NiB-CP	230	162
4	RuO_2	290	60

Fig. S19 Linear sweep voltammogram (*iR* corrected) for Fe_3O_4-70/Ni-foam.

Electrochemical surface area (ECSA):

The actual number of exposed sites of the catalyst during the electrochemical reaction was investigated by determining the electrochemicaly active surface area of different composites by calculating the double-layer pseudo-capacitance (C_{dl}). The cyclic voltammetry was recorded in the non-faradic potential region 1.13 V and 1.28 V *vs.* RHE with various scan rates (10 to 320 mV s^{-1}). The slope obtained from the graph averaged current density versus the scan rate the double-layer pseudo capacitance was determined. Thus, the ECSA was obtained by dividing C_{dl} by the specific capacitance of the flat standard surface (20-60 μF cm^{-2}), which is considered here 40 μF cm^{-2}.
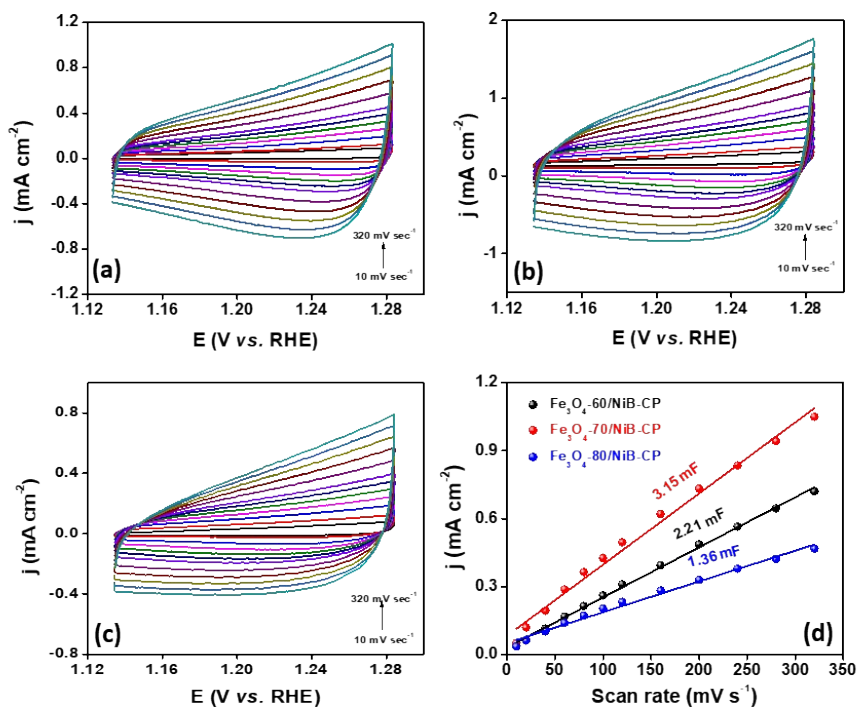
Fig. S20 Cyclic voltammograms for (a) Fe_3O_4-60/NiB-CP, (b) Fe_3O_4-70/NiB-CP (c) Fe_3O_4-80/NiB-CP electrodes in non-faradic potential region at various scan rates and (d) corresponding average current density *vs*. scan rate plot for ECSA determination.

Table S7 A. Electrochemical surface area of different electrodes.

S. No.	Composite	C_{dl} (mF)@ 1.24 V *vs*. RHE	ECSA (cm^2)
1	Fe_3O_4-60/NiB-CP	2.21	55.25
2	Fe_3O_4-70/NiB-CP	3.15	78.75
3	Fe_3O_4-80/NiB-CP	1.36	34

Electrochemical impedance measurements:

The electrochemical impedance spectroscopy study was performed by applying 1.43 V *vs.* RHE, DC potential over an AC perturbation of 10 mV with logarithmic frequency step over a single sine wave from 500 Hz to 10 mHz. The resulting Nyquist plot exhibited a semicircular behavior towards high frequency and a stout tail towards low frequency. The solution resistance (R_s) was obtained from the semicircle intersection at the real high-frequency axis, and the polarization resistance (R_p) at the low frequency near the electrode-electrolyte interface. The charge transfer resistance (R_{ct}) was calculated from the difference in R_p and R_s.
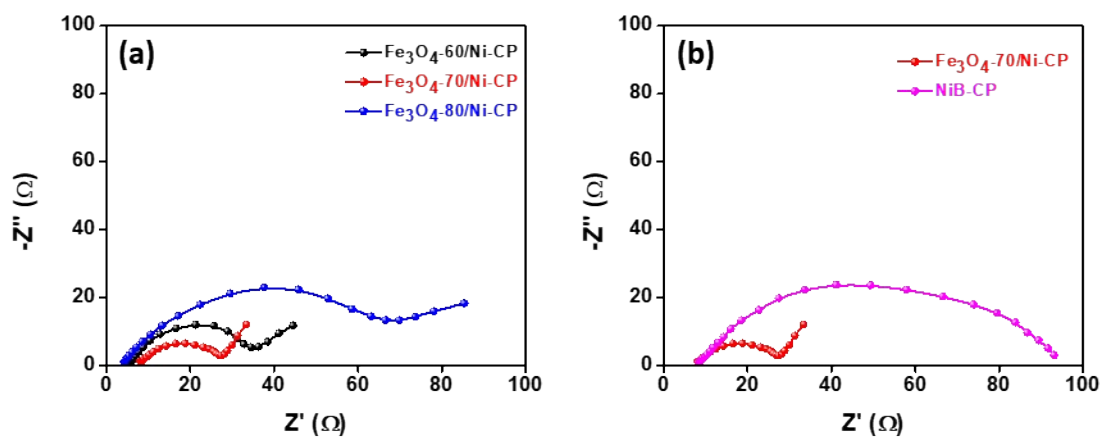
Fig. S21 Nyquist plot for (a) Fe_3O_4-T/NiB-CP electrodes and (b) NiB-CP and Fe_3O_4-70/NiB-CP electrodes.

Table S7 B. Electrochemical Impedance analysis for various electrodes extracted from Fig. S21.

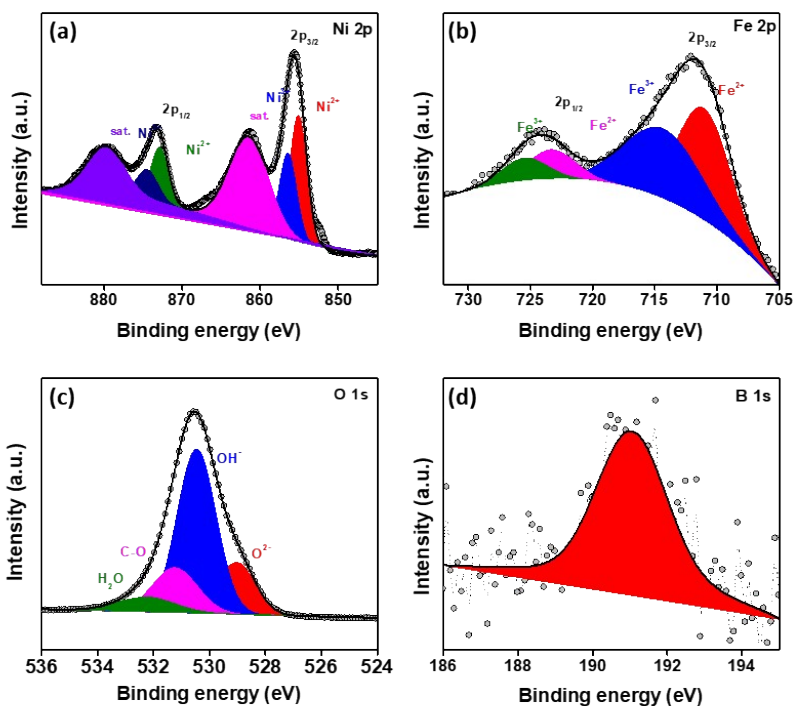| S.No.	Composites	R_s (Ω)	R_p (Ω)	R_{ct} (Ω)
1	Fe_3O_4-60/NiB-CP	6	34	28
2	Fe_3O_4-70/NiB-CP	7	27	20
3	Fe_3O_4-80/NiB-CP	5	67	62
4	NiB-CP	8	93	85

Fig. S22A XPS deconvoluted (a) Ni 2p, (b) Fe 2p, (c) O 1s and (d) B 1s spectrum obtained after OER stability tests.
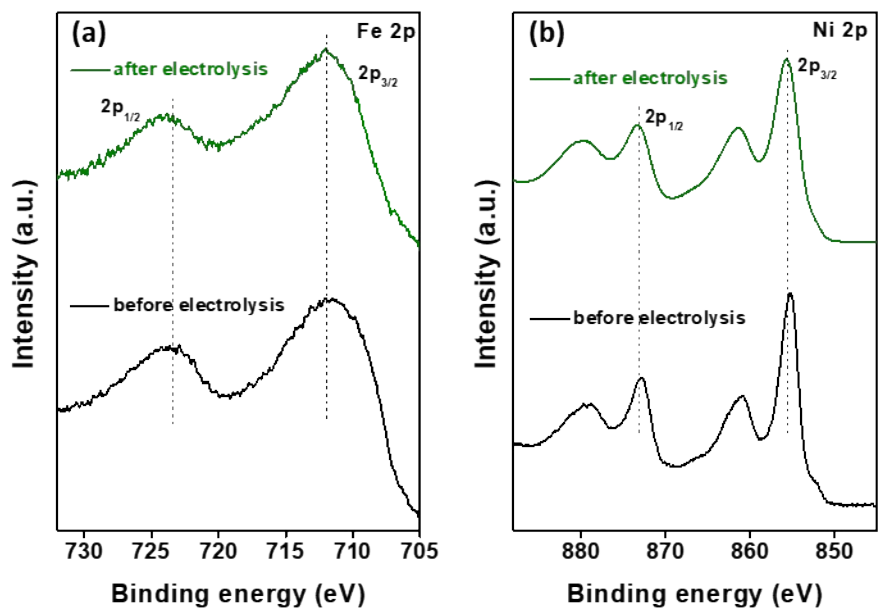
Fig. S22B XP spectra for Fe₃O₄-70/NiB-CP electrodes (a) Fe 2p and (b) Ni 2p before and after electrolysis.
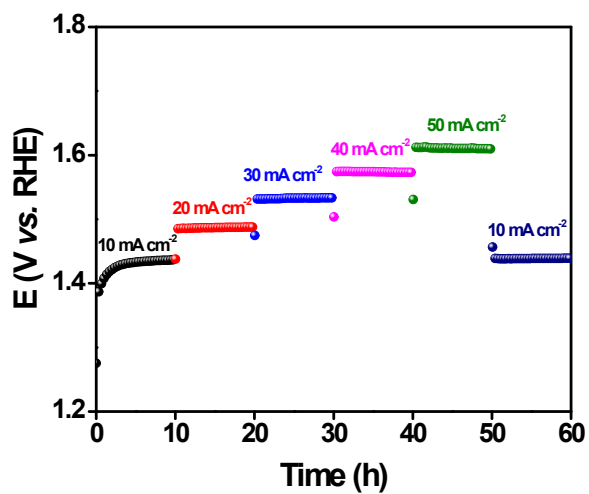

Fig. S23 Sequential chronopotentiometric measurements at different current densities for Fe₃O₄-70/NiB-CP respectively
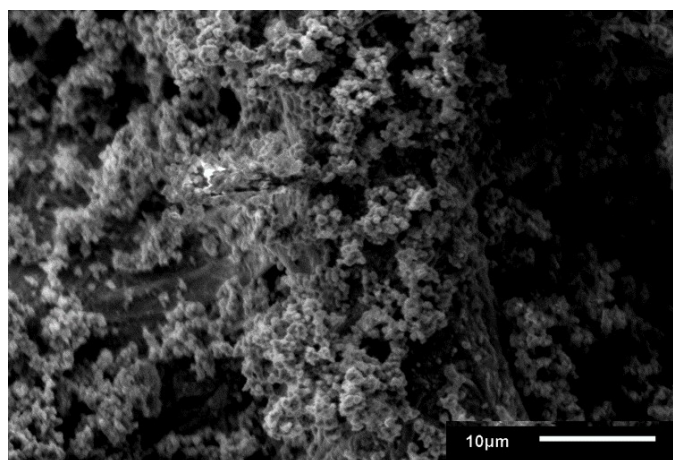
Fig. S24 A SEM image of Fe$_3$O$_4$-70/NiB-CP electrode after OER stability measurements.
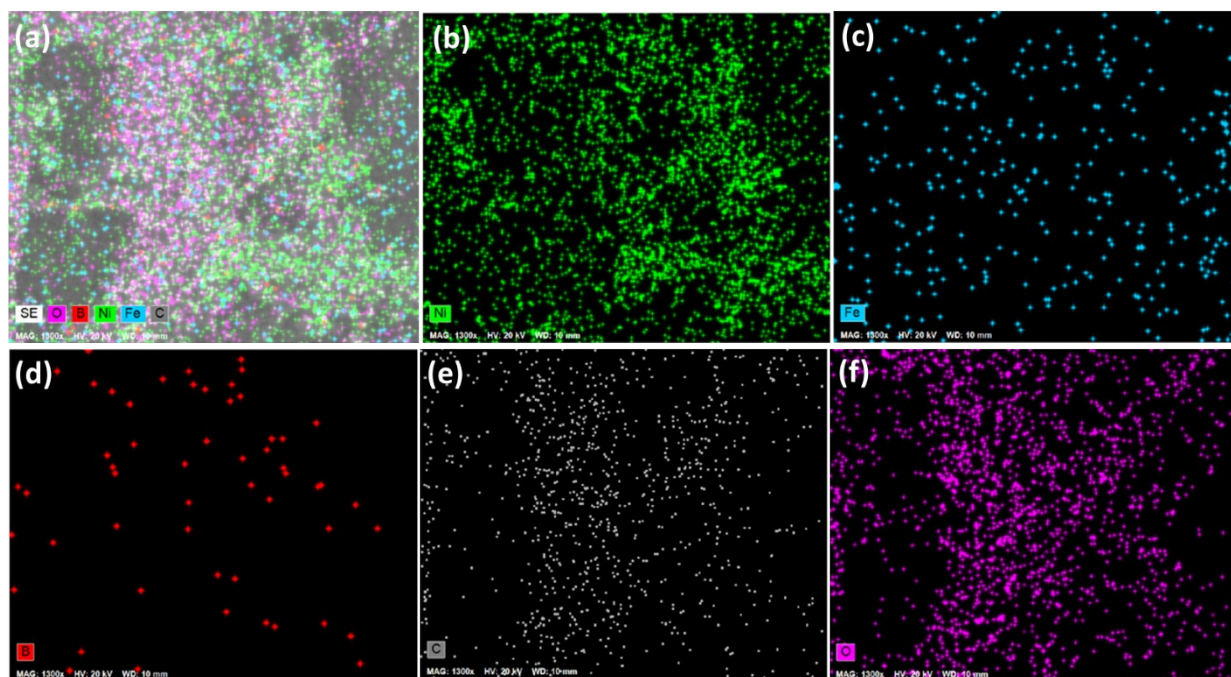
Fig. S24 B Elemental dot mapping image of Fe_3O_4-70/NiB-CP (a) for all elements and separately (b) Ni, (c) Fe (d) B (e) C and (f) oxygen after stability measurements.
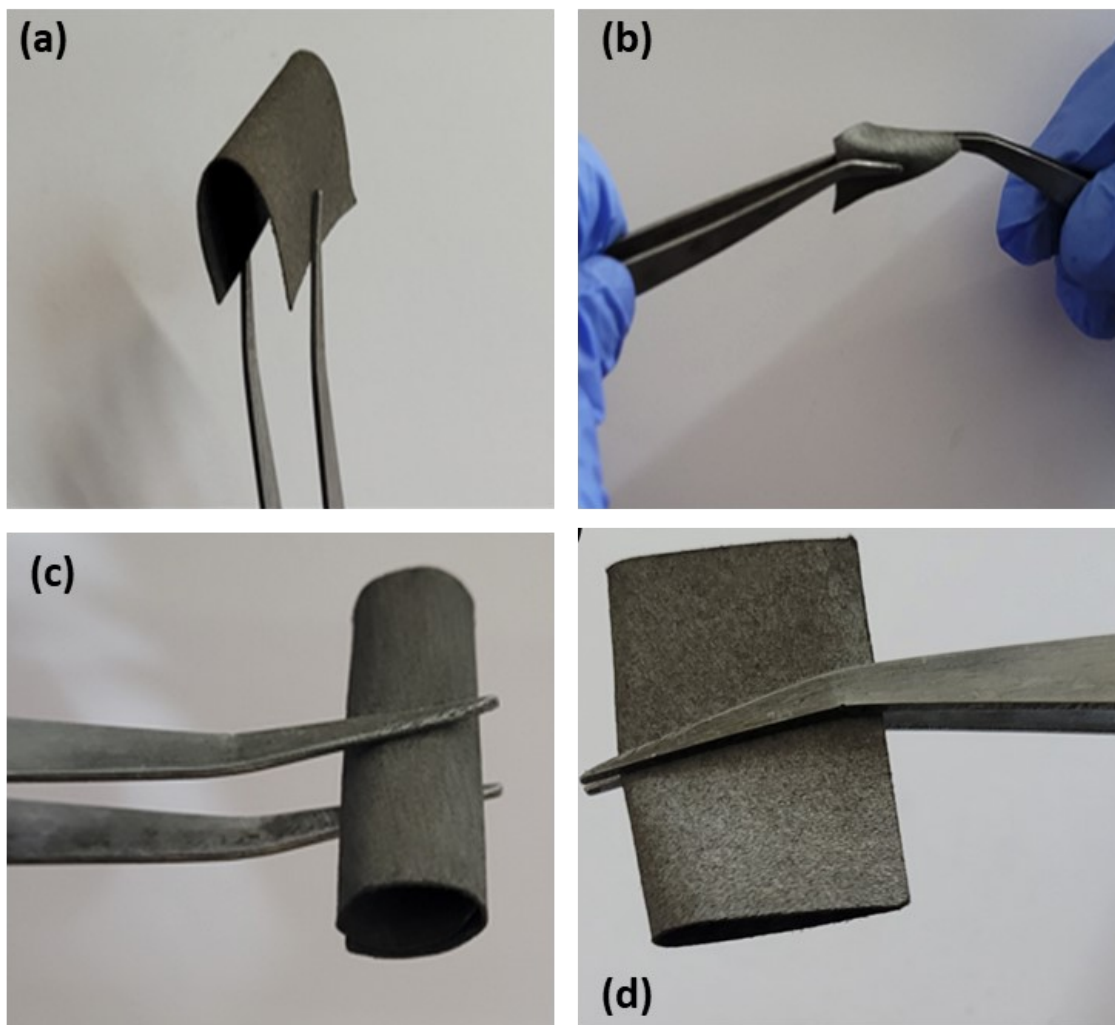

Fig. S25 Photographs of Fe_3O_4-70/NiB-CP electrodes showing high flexibility during (a) bending, (b) twisting (c) rolling and (d) folding deformation states.
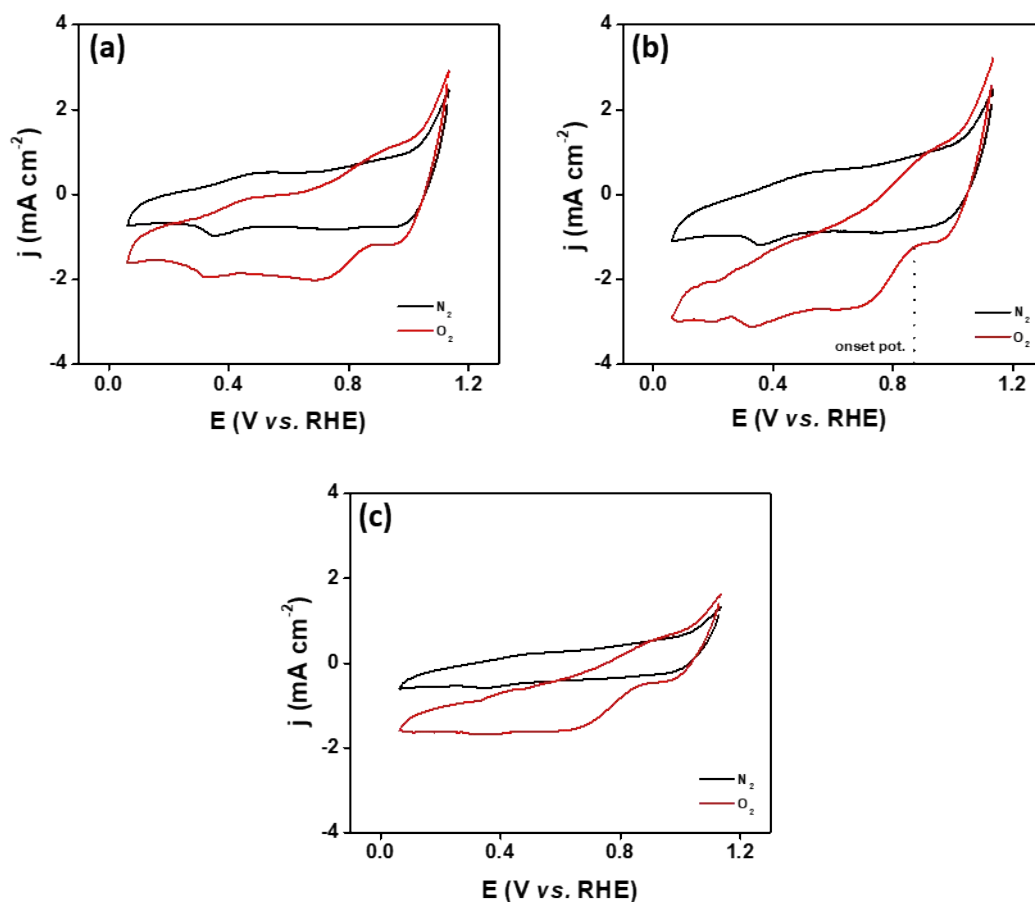
Fig. S26A Cyclic voltammogram of (a) Fe_3O_4-60/NiB-CP (b) Fe_3O_4-70/NiB-CP and (c) Fe_3O_4-80/NiB-CP electrodes in presence and absence of oxygen in 1 M KOH CE: Pt wire; RE: Hg/HgO/1M NaOH at a scan rate of at 25 mV s^{-1}.
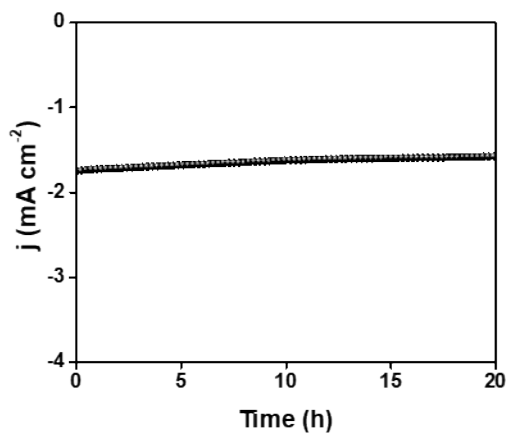
Fig. S26B Chronopotentiometric curve for Fe_3O_4-70/NiB-CP electrodes in oxygen saturated 1 M KOH.

Table S8. Comparison of onset potential for different composites.

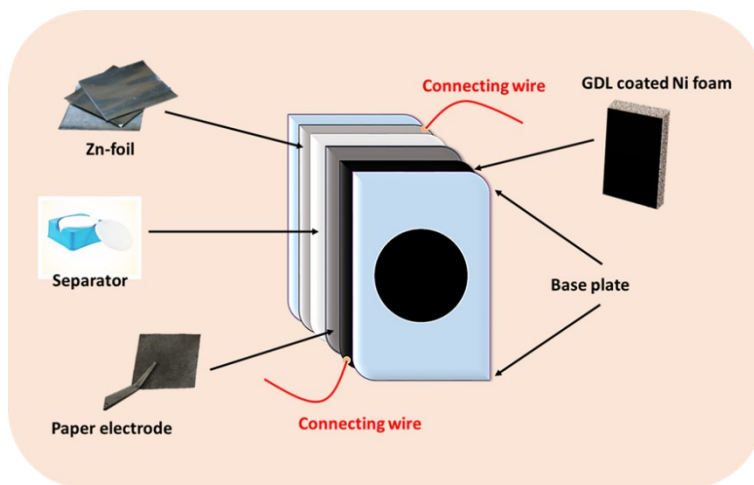| S.No.	Composites	Onset potential (V *vs.* RHE)
1	Fe_3O_4-60/NiB-CP	0.85
2	Fe_3O_4-70/NiB-CP	0.87
3	Fe_3O_4-80/NiB-CP	0.84

Fig. S27 Schematic representation of assembly of home-made Zn-O_2 battery.

Table S9. Comparison of peak power density with respect to amount of catalyst loaded for flexible Zn-O$_2$ battery with other reported literatures.

S.No.	Composite	Substrate	Peak power density (mW cm^{-2} mg$_{cat}$$^{-1}$)	References
1	CNT/Ag$_1$/ CNF	Cellulose Paper	70*	[14]
2	Co@NCNTA-700	Carbon cloth	38.6	[15]
3	NC-Co SA	Carbon cloth	22.96	[16]
4	NC-Co$_3$O$_4$	Carbon cloth	68.33#	[17]
5	Silk NC/KB	Carbon cloth	32.3	[18]
6	CC-AC	Carbon cloth	52.3$	[19]
7	Co/N@CNTs@CNMF-800	CNT macrofilm	125.5	[20]
8	Zn/Co-ZIFs/PAN	Carbon paper	69.6	[21]
9	**Fe$_3$O$_4$-70/NiB-CP**	**Cellulose Paper**	**300**	**This work**
10	Pt/C + RuO$_2$/NiB-CP	Cellulose Paper	326	This work

CNT/Ag$_1$/CNF: Carbon nanotube/cellulose nanofiber composite paper loaded with silver nanoparticles, **Co@NCNTAs**: cobalt NPs embedded in N-doped carbon nanotube arrays on CC, **NC-Co$_3$O$_4$-90**: Co$_3$O$_4$ nanospheres in nitrogen-doped carbon nanowall, **NC-Co SA**: nitrogen-doped porous carbon nanoflake arrays, **Silk NC/KB**: silk-derived defect-rich and nitrogen-doped nanocarbon, **CC-AC**: activated commercial carbon cloth, **Co/N@CNTs@CNMF-800**: cobalt nanoparticles embedded nitrogen-rich carbon nanotubes. * mW cm^{-2}, # mW cm^{-3} mg$_{cat}$$^{-1}$, $ mW cm^{-3}
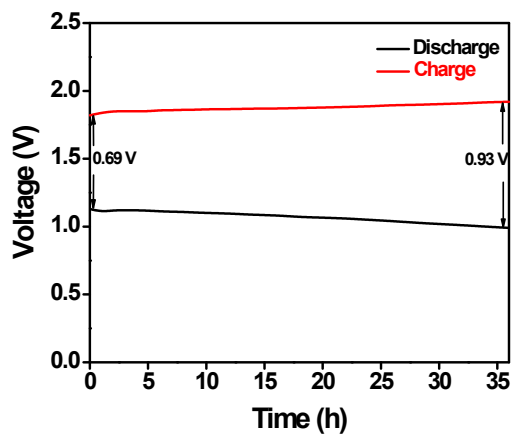
Fig. S28A Potential variation study with respect to time during prolonged charge-discharge cycles.
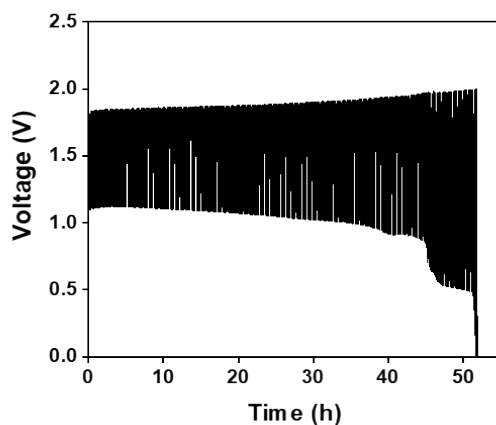

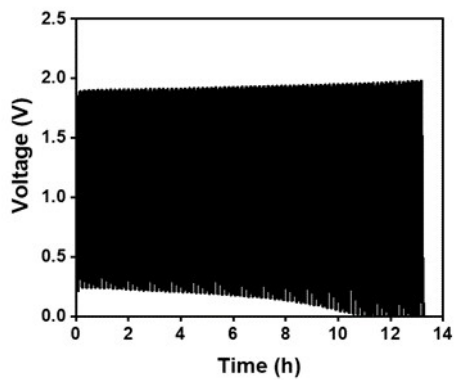**Fig. S28B** Battery cycling performance at current density of 5 mA cm^{-2} till failure.

Fig. S28C Battery cycling performance at 5 mA cm^{-2} with used air cathode (after stability) and fresh anode, GDL, separator.
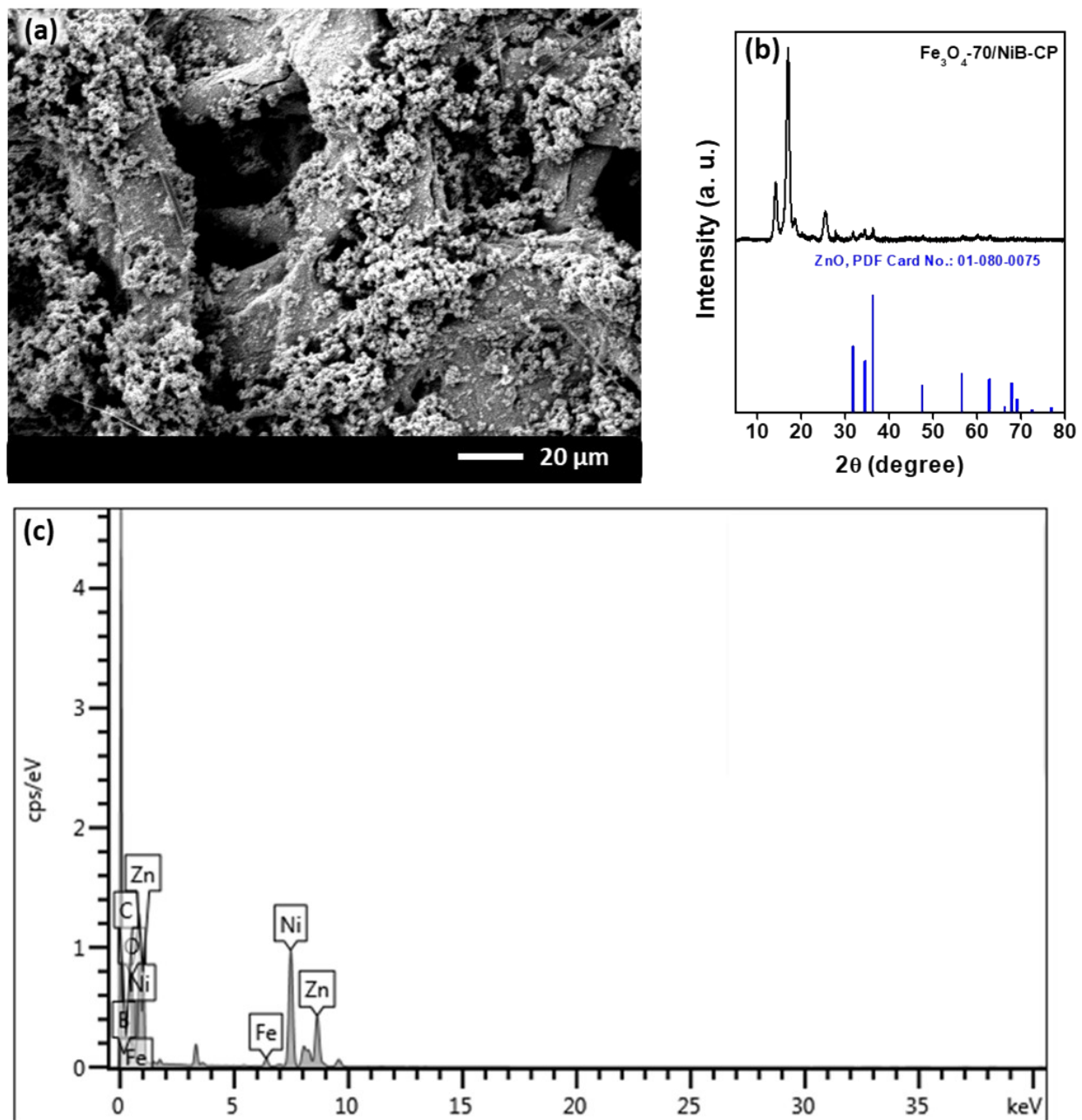
Fig. S28D (a) SEM image, (b) P-XRD pattern, (c) EDS spectrum for Fe$_3$O$_4$-70/NiB-CP air cathode collected after long-term battery cycling and subsequent failure.
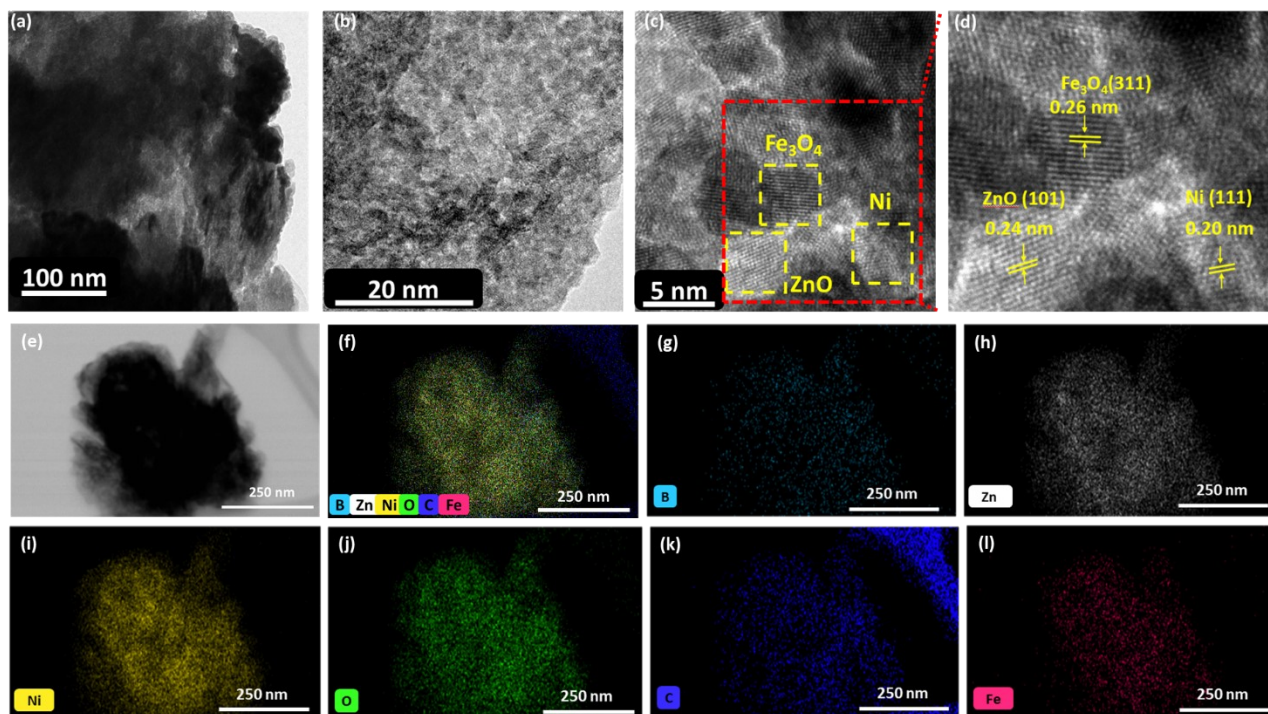
Fig. S28E (a) TEM image, (b-d) HR-TEM images with presence of lattice fringes related to Fe_3O_4, Ni and ZnO and (e-l) TEM EDS spectrum for Fe_3O_4-70/NiB-CP air cathode collected after long-term battery cycling and subsequent failure.
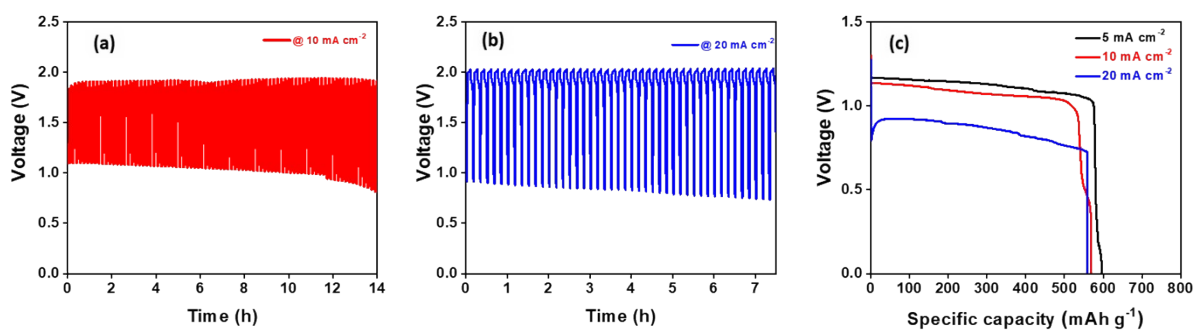
Fig. S28F (a) Long-term cycling stability of Fe_3O_4-70/NiB-CP equipped Zn-air battery at 10 mA cm^{-2} and (b) 20 mA cm^{-2} of current density respectively. (c) Comparison of rate performance of air cathode in terms of specific capacity at different current densities.
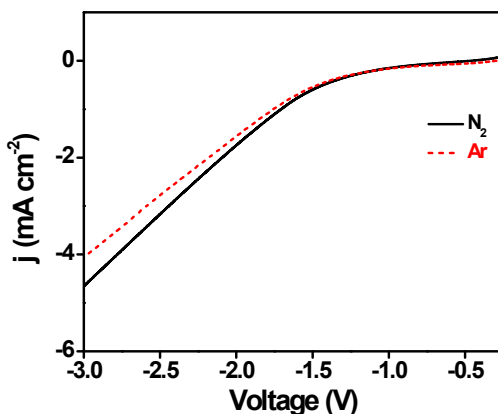

Fig. S29 LSV curve acquired during full cell study of Fe_3O_4-70/NiB-CP// Fe_3O_4-70/NiB-CP
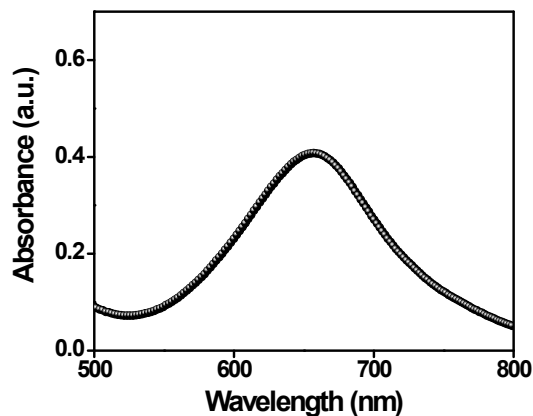

Fig. S30 UV-vis spectrum recorded for quantification of ammonia formed when powered by Zn-O_2 battery.

References

1.   D. K. Schroder, *Semiconductor material and device characterization*, John Wiley & Sons, 2015.

2.   W. Liu, C. Li, Q. Xu, P. Yan, C. Niu, Y. Shen, P. Yuan and Y. Jia, *ChemCatChem*, 2019, **11**, 5412-5416.
3.   Y. Zhao, R. Shi, X. Bian, C. Zhou, Y. Zhao, S. Zhang, F. Wu, G. I. Waterhouse, L. Z. Wu and C. H. Tung, *Adv. Sci.*, 2019, **6**, 1802109.
4.   W. Li, T. Wu, S. Zhang, Y. Liu, C. Zhao, G. Liu, G. Wang, H. Zhang and H. Zhao, *Chem. Commun.*, 2018, **54**, 11188-11191.
5.   G. Liu, C. Zhao and S. Ding, *New J. Chem.*, 2020, **44**, 21070-21075.
6.   S. Cheng, C. Li, Z. Yu, Y. Sun, L. Li and J. Yang, *RSC Adv.*, 2020, **10**, 9814-9823.
7.   Z. Wang, K. Zheng, S. Liu, Z. Dai, Y. Xu, X. Li, H. Wang and L. Wang, *ACS Sustain. Chem. Eng.*, 2019, **7**, 11754-11759.
8.   G. Li, Z. Pan, H. Lin and L. An, *J. Alloys Compd.*, 2021, **875**, 160006.
9.   X. Chen, Y.-T. Liu, C. Ma, J. Yu and B. Ding, *J. Mater. Chem. A*, 2019, **7**, 22235-22241.
10.   X. Zhao, X. Zhang, Z. Xue, W. Chen, Z. Zhou and T. Mu, *J. Mater. Chem. A*, 2019, **7**, 27417-27422.
11.   X. Zhang, R.-M. Kong, H. Du, L. Xia and F. Qu, *Chem. Commun.*, 2018, **54**, 5323-5325.
12.   J. Zhang, X. Tian, M. Liu, H. Guo, J. Zhou, Q. Fang, Z. Liu, Q. Wu and J. Lou, *J. Am. Chem. Soc.*, 2019, **141**, 19269-19275.
13.   L. Li, C. Tang, D. Yao, Y. Zheng and S.-Z. Qiao, *ACS Energy Lett.*, 2019, **4**, 2111-2116.
14.   S. Li, W. Zhao, N. Zhang, Y. Luo, Y. Tang, G. Du, C. Wang, X. Zhang and L. Li, *Energy Fuels*, 2021, **35**, 9017-9028.
15.   L. Liu, Y. Wang, F. Yan, C. Zhu, B. Geng, Y. Chen and S. l. Chou, *Small Methods*, 2020, **4**, 1900571.
16.   W. Zang, A. Sumboja, Y. Ma, H. Zhang, Y. Wu, S. Wu, H. Wu, Z. Liu, C. Guan and J. Wang, *ACS Catal.*, 2018, **8**, 8961-8969.
17.   C. Guan, A. Sumboja, H. Wu, W. Ren, X. Liu, H. Zhang, Z. Liu, C. Cheng, S. J. Pennycook and J. Wang, *Adv. Mater.*, 2017, **29**, 1704117.
18.   C. Wang, N.-H. Xie, Y. Zhang, Z. Huang, K. Xia, H. Wang, S. Guo, B.-Q. Xu and Y. Zhang, *Chem. Mater.*, 2019, **31**, 1023-1029.
19.   K. Kordek, L. Jiang, K. Fan, Z. Zhu, L. Xu, M. Al-Mamun, Y. Dou, S. Chen, P. Liu and H. Yin, *Adv. Energy Mater.*, 2019, **9**, 1802936.
20.   T. Liu, J. Mou, Z. Wu, C. Lv, J. Huang and M. Liu, *Adv. Funct. Mater.*, 2020, **30**, 2003407.
21.   Q. Niu, B. Chen, J. Guo, J. Nie, X. Guo and G. Ma, *Nano-Micro Lett.*, 2019, **11**, 1-17.